COMMUNICATION

ADVANCED MATERIALS
www.advmat.de

Asymmetric Air Cathode Design for Enhanced Interfacial Electrocatalytic Reactions in High-Performance Zinc–Air Batteries

*Jia Yu, Bo-Quan Li, Chang-Xin Zhao, Jia-Ning Liu, and Qiang Zhang**

The rechargeable zinc–air battery (ZAB) is a promising energy storage technology owing to its high energy density and safe aqueous electrolyte, but there is a significant performance bottleneck. Generally, cathode reactions only occur at multiphase interfaces, where the electrocatalytic active sites can participate in redox reactions effectively. In the conventional air cathode, the 2D multiphase interface on the surface of the gas diffusion layer (GDL) inevitably results in an insufficient amount of active sites and poor interfacial contact, leading to sluggish reaction kinetics. To address this problem, a 3D multiphase interface strategy is proposed to extend the reactive interface into the interior of the GDL. Based on this concept, an asymmetric air cathode is designed to increase the accessible active sites, accelerate mass transfer, and generate a dynamically stabilized reactive interface. With a NiFe layered-double-hydroxide electrocatalyst, ZABs based on the asymmetric cathode deliver a small charge/discharge voltage gap (0.81 V at 5.0 mA cm^{-2}), a high power density, and a stable cyclability (over 2000 cycles). This 3D reactive interface strategy provides a feasible method for enhancing the air cathode kinetics and further enlightens electrode designs for energy devices involving multiphase electrochemical reactions.

Owing to the current environmental crisis and increasing energy demands, great efforts have been made to develop efficient energy storage devices based on renewable sources.[1] Rechargeable zinc–air batteries (ZABs) have demonstrated considerable potential in portable and large-scale power supply and storage applications because of their various advantages (e.g., a high theoretical energy density (1086 Wh kg^{-1}), a safe aqueous electrolyte, and abundant zinc resource).[2] The main components of a ZAB are a metal Zn anode and an air cathode packaged together with an aqueous alkaline electrolyte, as illustrated in Figure S1 (Supporting Information). The air cathode consists of oxygen electrocatalysts integrated on a hydrophilic substrate and a hydrophobic gas diffusion layer (GDL), to promote both the oxygen reduction reaction (ORR) and the oxygen evolution reaction (OER).[3] However, the sluggish reaction kinetics of this component usually hinders the energy efficiency and output power of ZABs.[4] Therefore, the key to overcoming the performance bottleneck of ZABs is the fabrication of high-efficiency air cathodes, in which the intrinsic electrocatalyst activity and interfacial engineering play equally critical roles. Recently, a series of novel electrocatalysts with excellent intrinsic ORR/OER activities was proposed, including noble-metal-based catalysts and their cost-effective alternatives (e.g., carbon-based materials, transition metal oxides/chalcogenides/hydroxides, and hybrids of these materials).[5] Their intrinsic activities can be further optimized by morphology regulation, defect creation, and electronic structure modulation to promote the reaction kinetics.[6]

However, in an air cathode, electrochemical reactions that involve gases occur predominantly in the multiphase interface region among the solid electrocatalysts, the liquid electrolyte, and oxygen.[7] This means only accessible electrocatalysts in the interface region are fully functional. Therefore, the effective utilization of electrocatalysts with high intrinsic activities necessitates a multiphase interface with abundant and stable electrocatalytic active sites. Despite this requirement, the interfacial engineering of air cathodes has received little attention.[8] Conventional air cathodes applied in two-electrode rechargeable ZABs are fabricated by loading a hydrophilic bifunctional electrocatalyst layer on the surface of a hydrophobic GDL via a drop-casting or spray-coating method, for constructing multiphase reactive interfaces (**Figure 1**a).[9] However, this cathode structure provides a nearly 2D multiphase interface that is confined to the narrow space between the electrocatalyst layer and the GDL. As this 2D interface is accessible to only a small proportion of the electrocatalysts located near the GDL surface, most of the catalytic sites cannot make an actual contribution. Thus, it results in an insufficient amount of active sites and slow mass transfer in the ORR/OER processes. Moreover, even the functional active sites suffer from

Dr. J. Yu, B.-Q. Li, C.-X. Zhao, J.-N. Liu, Prof. Q. Zhang
Beijing Key Laboratory of Green Chemical Reaction Engineering and Technology
Department of Chemical Engineering
Tsinghua University
Beijing 100084, China
E-mail: zhang-qiang@mails.tsinghua.edu.cn

The ORCID identification number(s) for the author(s) of this article can be found under https://doi.org/10.1002/adma.201908488.

DOI: 10.1002/adma.201908488

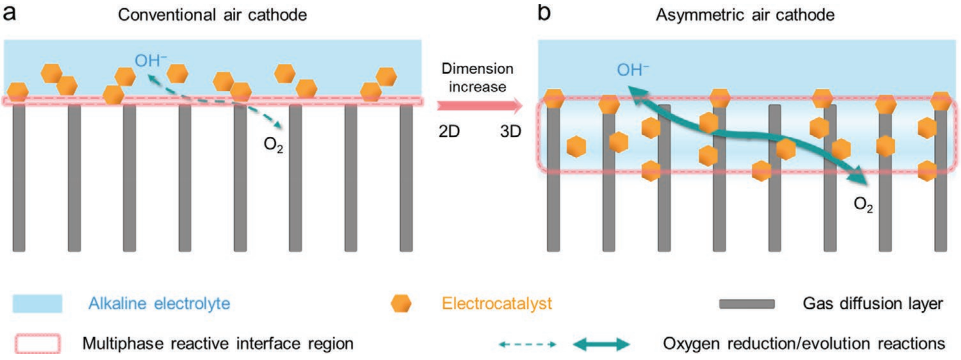

Figure 1. a,b) Schematic illustrations of conventional (a) and asymmetric (b) air cathodes, which possess 2D and 3D multiphase reactive interfaces, respectively. The asymmetric air cathode exhibits an increased amount of active sites, accelerated mass transfer, and a dynamically stabilized reactive interface.

poor contact with the reactive interface and can easily fall into the electrolyte during redox reactions.[10] Therefore, the conventional air cathode structure inevitably gives rise to sluggish and unstable reaction kinetics, which greatly hinders battery performance.

To overcome the limitations of the 2D reactive interface, for the first time we propose a dimension-increasing interfacial strategy. Its core idea is to extend the original 2D multiphase interface toward the GDL to construct a 3D multiphase reactive interface inside the GDL. When compared with the 2D interface, which is limited to the GDL surface, the 3D reactive interface can significantly increase the amount of active sites and accelerate mass transfer owing to its extended and interconnected interfacial structure.[11] Moreover, a dynamically balanced reactive region with superior mechanical stability is obtained.[12] Even if some electrocatalysts fall off and migrate within the 3D interfacial region, they are still able to function. Accordingly, the 3D interface is expected to offer considerable advantages for the cathode kinetics.

To realize the 3D multiphase reactive interface, we designed an asymmetric air cathode structure inspired by natural leaves, which are asymmetric photocatalytic systems. The upper palisade layer of a leaf supports the photosynthetic active sites while the lower spongy layer mainly executes gas exchange (Figure S2, Supporting Information). Similarly, in our asymmetric cathode design, the oxygen electrocatalysts are grown from one face of the GDL toward the interior to achieve a certain thickness, while the rest of the GDL maintains its original structure (Figure 1b). As this structure allows simultaneous electrolyte permeation and oxygen diffusion within the conductive skeleton, an internal 3D multiphase interface is achieved. The ZAB based on this asymmetric air cathode delivers a lower overpotential, a higher power density, and a more stable cyclability than that based on a conventional air cathode.

As a proof of concept, an asymmetric air cathode (hereinafter referred to as Asy-cathode) based on NiFe layered-double-hydroxide (NiFe-LDH) electrocatalysts was constructed via a liquid-phase chemical process, as illustrated in Figure S3 (Supporting Information). Among noble-metal-free alternatives, NiFe-LDH is one of the best OER electrocatalysts owing to its high abundance and outstanding catalytic activity; however, its intrinsic ORR activity is unsatisfactory.[13] As the ORR is a gas-consuming process, it is more sensitive to the multiphase interface than OER; thus, NiFe-LDH is regarded as an ideal material to verify the effectiveness of the asymmetric cathode design.[14] Briefly, precisely controlled single-face pretreatment produced a Janus carbon fiber paper (CFP) with one hydrophilic and one hydrophobic face, which subsequently served as both the growth substrate and GDL. Using a mild float-growth method, NiFe-LDH was grown inward from the hydrophilic face of the CFP to produce an oxygen electrocatalytic face (OCF), while the hydrophobic face remained unchanged as a gas diffusion face (GDF).

To confirm the successful construction of the desired asymmetric structure, the differences in morphologies, components and properties between the OCF and the GDF were characterized using various techniques. First, optical photographs show that the two faces of Asy-cathode are different colors, as shown in **Figure 2**a. The brownish yellow color of OCF indicates the growth of NiFe-LDH, while the GDF maintains the pristine black color of CFP. The fine morphological features of the two faces were investigated by scanning electron microscopy (SEM). On the OCF, the growth of a large number of nanostructures which coat the internal carbon fibers and partly fill the void is observed (Figure 2b; Figure S4a,b, Supporting Information). Owing to the hydrophilicity of hydroxides, this growth mode can induce good electrolyte infiltration, which will promote the accessibility of hydroxide ions and oxygen inside cathode to extend the reactive interface. In contrast, on the GDF, only carbon fibers are observed accompanied by some polytetrafluoroethylene (PTFE) components, which play a key role in maintaining hydrophobicity (Figure 2c; Figure S4c,d, Supporting Information).

Raman spectroscopy was performed to further identify the chemical components on the two faces of Asy-cathode (Figure 2d). The spectrum of OCF clearly shows the characteristic peaks of brucite-like $Ni(OH)_2$ as well as a peak corresponding to incorporated FeOOH (Fe^{3+}), which indicates low crystallinity.[15] Meanwhile the peak at 1075 cm^{-1} indicates the presence of intercalated carbonate ions.[16] In contrast, the spectrum of GDF exhibits no obvious peaks at the above bands, verifying that the chemical components on the two faces are completely different.

In addition, the asymmetry of the wettability characteristics of Asy-cathode was investigated using contact angle

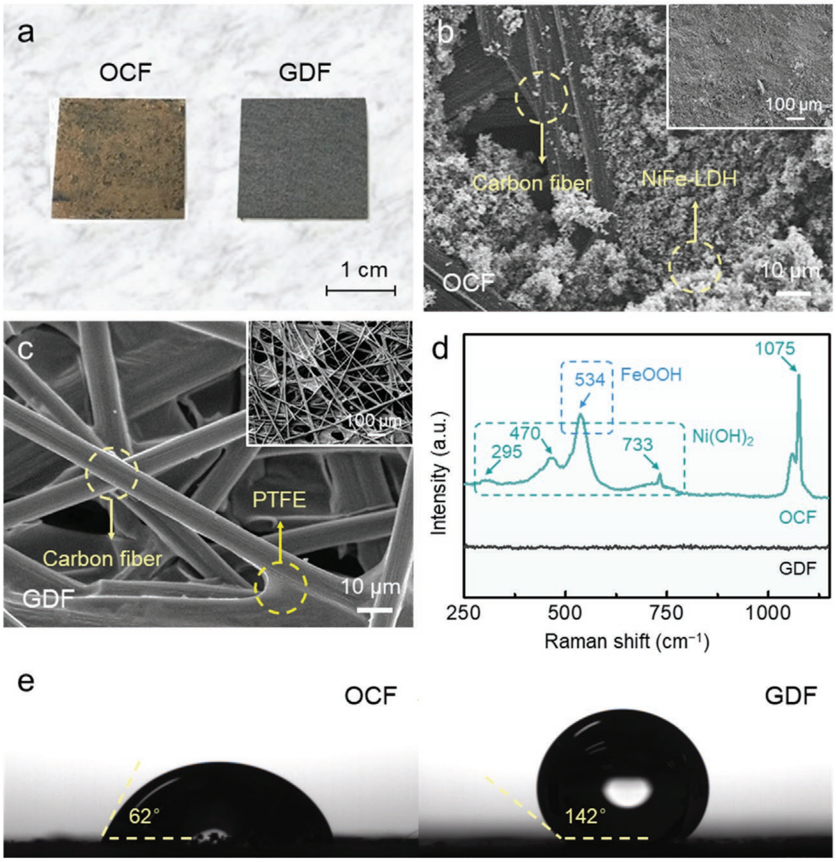

Figure 2. Characterizations of the two faces of Asy-cathode. a) Optical photographs and b,c) SEM images of the OCF and the GDF showing asymmetric morphological features. d) Raman spectra showing asymmetric chemical components. e) Contact angles with the ZAB electrolyte showing asymmetric wettability characteristics.

measurements, as this factor is of great importance for the practical application of air cathodes in ZABs (Figure 2e). The OCF exhibits a much smaller contact angle (62°) with the ZAB electrolyte (6.0 M KOH + 0.20 M Zn(Ac)$_2$) than the GDF (142°). Thus, the electrolyte can easily wet OCF and partly fill the inner pores, but complete soaking of the cathode is avoided and fluent gas diffusion from the opposite GDF is ensured. In this way, an enhanced multiphase interface is created inside the cathode.[17] As a comparison, the surface morphology and contact angle data of the pristine CFP are shown in Figures S5 and S6 (Supporting Information), respectively. Compared with those of the pristine CFP, both the structure and wettability of OCF of Asy-cathode were completely transformed. However, the hydrophobicity of GDF was well maintained, although the PTFE coating layer was partly damaged.

To investigate the reactive interface within the Asy-cathode, the interior architecture was visualized by cross-sectional SEM (**Figure 3**a). Ultrafine nanoparticles are observed in the upper half of Asy-cathode, while pristine carbon fibers are maintained in the lower half, clearly demonstrating the heterojunction boundary between the OCF and the GDF. The element distributions revealed by electron probe X-ray microanalysis (EPMA) and energy dispersive spectroscopy (EDS) mapping also confirmed the asymmetric architecture of Asy-cathode. As shown in Figure 3b and Figure S7 (Supporting Information), the OCF in the upper half is rich in Ni, Fe, O, and C, whereas the GDF in the lower half only contains C.

To observe the multiphase reactive interface directly, sophisticated interior structure of Asy-cathode was further visualized by 3D X-ray computed tomography (CT). Figure 3c shows the 3D tomogram sliced along a cross section, and the detailed reconstructed animation is shown in Movie S1 (Supporting Information). The metal-based electrocatalysts are clearly observed to grow on one face and inside the CFP. As illustrated in Figure 3d, rather than poor 2D interface of the conventional cathode, the asymmetric cathode is proposed to achieve a 3D multiphase reactive interface through the growth of electrocatalysts into the interior of the GDL, which enhances the access of the electrolyte and gases. Taking advantage of the increased number of active sites and accelerated mass transfer, the Asy-cathode should exhibit enhanced kinetics compared with the conventional air cathode. Therefore, a higher electrocatalytic activity and improved battery performance are expected.

Additional characterizations were performed to investigate the properties of the entire Asy-cathode. The X-ray diffraction (XRD) patterns confirmed the successful growth of NiFe-LDH (Figure S8, Supporting Information). For the XRD pattern of the electrocatalysts scraped from Asy-cathode, the main characteristic peaks are indexed to the (003), (006), (012), and (110) lattice planes of NiFe-LDH (JCPDS card no. 40-0125), whereas the broad peak shape indicates low crystallinity and a relatively small crystallite size.[18] As the grown NiFe-LDH only accounts for a small proportion of the cathode, the XRD pattern of the entire Asy-cathode sample mainly demonstrates peaks corresponding to the CFP. X-ray photoelectron spectroscopy (XPS) was also performed on the Asy-cathode. The survey spectrum exhibits Ni, Fe, O, and C signals, which are consistent with the above EPMA and EDS mapping results (Figure S9, Supporting Information).[19] In addition to these elements, a F signal was also detected owing to the existence of PTFE.

The air cathode plays a significant role in ZAB performance.[20] To evaluate the effectiveness of Asy-cathode, we also fabricated a conventional air cathode with the same NiFe-LDH electrocatalysts and identical mass loading (hereinafter referred to as Con-cathode; Figure S10, Supporting Information). Briefly, a hydrophilic carbon cloth (CC) and a hydrophobic CFP were composited using a hot press, and then the electrocatalysts were loaded on the CC side via a controlled drop-casting method. The as-constructed multiphase interface between the electrocatalyst/CC and CFP is 2D, and thus the Con-cathode serves as an ideal control sample. As illustrated in Figure S11 (Supporting Information), the accessible

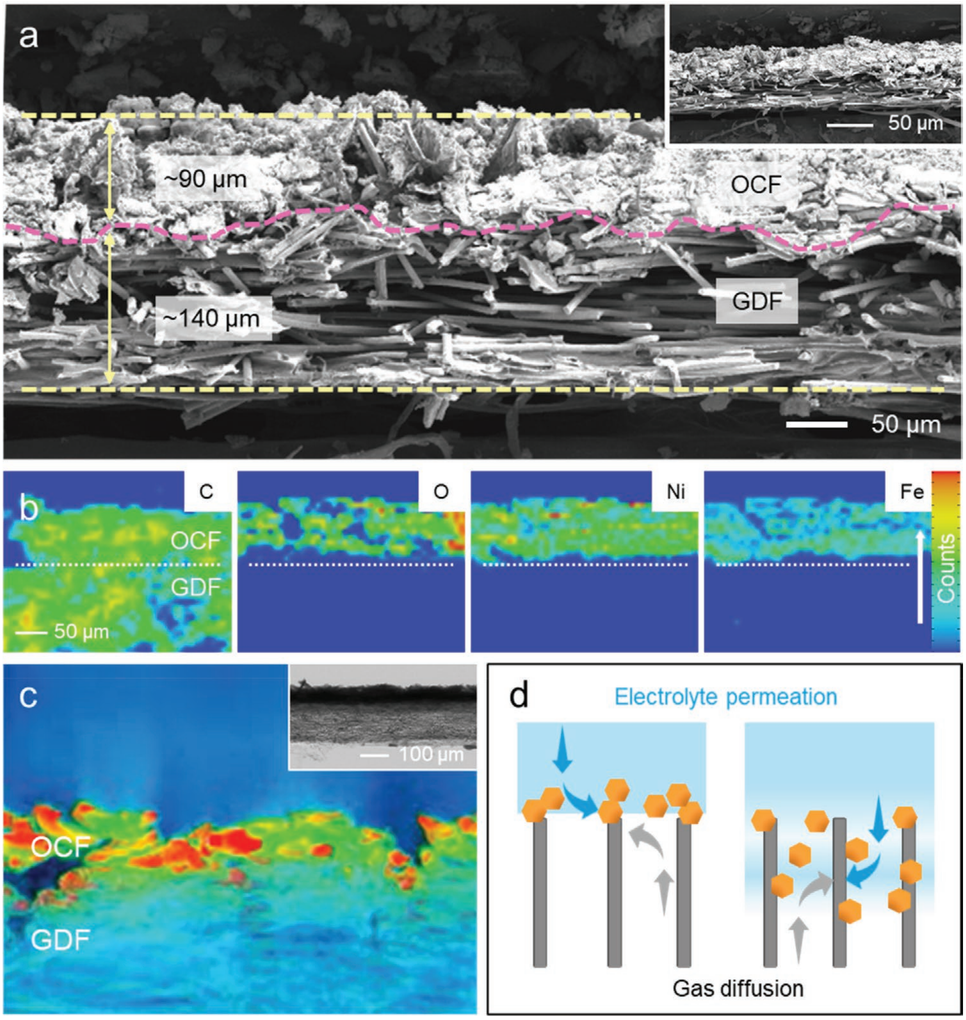

Figure 3. Characterizations of the 3D interface in Asy-cathode. a) Cross-sectional SEM images demonstrating the heterojunction boundary between the OCF and the GDF. b) EPMA mapping patterns of C, O, Ni, and Fe elements. c) CT 3D tomogram sliced along a cross section. d) The multiphase reactive interface advantage of the asymmetric cathode (right) over the conventional cathode (left).

electrocatalysts are loaded on the 2D interface in Con-cathode, which is distinct from the 3D electrocatalyst architecture in Asy-cathode. To compare the electrocatalytic performance, both cathodes were tested in ZABs with Zn foil as the anode and 6.0 M KOH + 0.20 M $Zn(Ac)_2$ solution as the electrolyte.

Figure 4a compares the polarization curves of the ZABs based on Asy-cathode and Con-cathode at a scan rate of 10.0 mV s^{-1}. The voltages required for the ZAB with Asy-cathode to achieve 25.0 mA cm^{-2} discharge and charge current densities are 0.94 and 1.93 V, respectively, while those for the ZAB with Con-cathode are 0.84 and 1.96 V, respectively. Moreover, the maximum discharge power densities (P_{max}) of the ZABs with Asy-cathode and Con-cathode are 93.9 and 42.1 mW cm^{-2}, respectively. Clearly, the Asy-cathode is greatly superior to the Con-cathode. In particular, the remarkable P_{max} of the ZAB with Asy-cathode can be attributed to the presence of sufficient active sites and efficient mass transfer, as mass-transfer-related concentration polarization will dominate ZAB performance at a high current density.[21] To exemplify the practical applicability of the Asy-cathode design, two as-assembled ZABs with Asy-cathode were used to power a light-emitting diode (LED) (Figure S12, Supporting Information). Furthermore, the specific capacities were tested at a discharge current density of 25.0 mA cm^{-2} and normalized to the mass of Zn anodes (Figure S13, Supporting Information). The specific capacity of the ZAB with Asy-cathode (800 mA h g_{Zn}^{-1}) is higher than that of the ZAB with Con-cathode (749 mA h g_{Zn}^{-1}).

To evaluate the effect of the asymmetric architecture on ORR/OER kinetics, discharge–charge curves were collected for the ZABs based on Asy-cathode and Con-cathode at various current densities, as presented in Figure 4b. Obviously, the Asy-cathode provides the ZAB with a smaller charge/discharge voltage gap which indicates lower polarization and a higher energy efficiency, especially at high current densities. When the current density increases from 5.0 to 25.0 mA cm^{-2}, the charge voltage with Asy-cathode shows a slight increase from 1.93 to 1.98 V, whereas that with Con-cathode increases considerably from 1.96 to 2.08 V. Even at 50.0 mA cm^{-2}, the former still retains a charge voltage of 2.06 V, which is approximately 210 mV lower than that of the latter. Compared with the charge

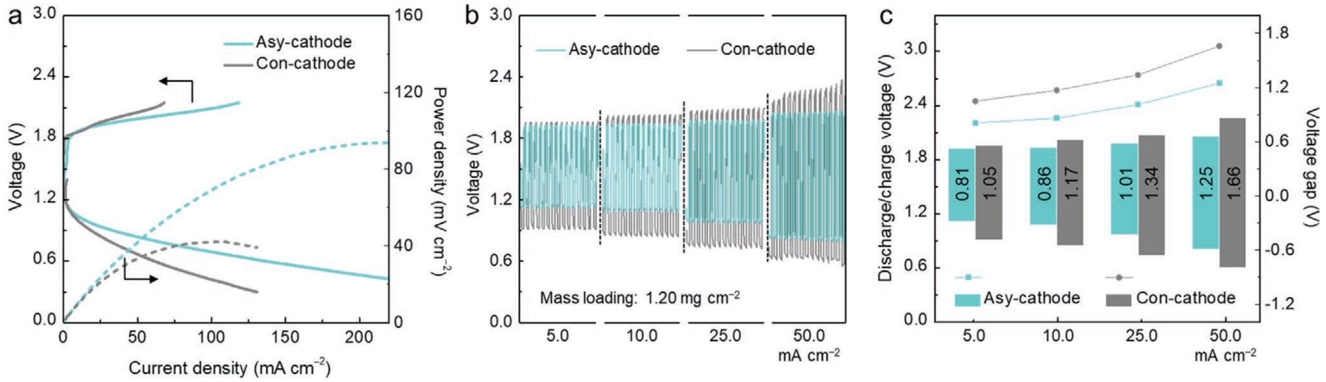

Figure 4. Electrochemical performance of the ZABs with Asy-cathode and Con-cathode. a) Discharge/charge polarization and power density curves. b) Discharge–charge curves at various current densities and c) corresponding average discharge/charge voltages and voltage gaps.

process, the discharge process is more affected by the different multiphase interfaces. The discharge voltage of the ZAB with Con-cathode is only 0.91 V at 5.0 mA cm^{-2} owing to the poor ORR activity of NiFe-LDH, but that of the ZAB with Asy-cathode reaches 1.12 V. More importantly, the advantageous effect of Asy-cathode becomes more obvious as the current density increases. As the ORR process is highly sensitive to the multiphase interface, the Asy-cathode benefits more from its higher discharge voltage, revealing the huge advantage of the asymmetric architecture in terms of kinetics.[22] Moreover, the average discharge/charge voltage and voltage gap values are presented in Figure 4c. Although the polarization intensifies as the current density increases, the ZAB based on Asy-cathode demonstrates relatively small voltage gaps of 0.81, 0.86, 1.01, and 1.25 V at 5.0, 10.0, 25.0, and 50.0 mA cm^{-2}, respectively, while those for the ZAB with Con-cathode are 1.05, 1.17, 1.34, and 1.66 V, respectively. These results suggest the excellent application potential of the asymmetric air cathode under high current conditions.

Obviously, the enhanced multiphase reactive interface of Asy-cathode largely improves the catalytic activity of NiFe-LDH electrocatalysts. With an asymmetric architecture, it can facilitate transfer of hydroxide ions and oxygen to realize efficient ORR/OER on the surface and in the interior of the CFP. However, the electrocatalytic reactive region of Con-cathode is limited to the surface in contact with the electrolyte. As is well known, the discharge and charge voltages of ZABs correspond to the air cathode polarization during the ORR and OER processes, respectively, while the voltage gap represents the bifunctional activity to a great extent.[23] Therefore, within the Asy-cathode, the inherently weak ORR activity of NiFe-LDH can be significantly enhanced to achieve the ORR/OER bifunctionality required for ZAB applications.[24]

The cycling performance of an air cathode is determined by the stability of its multiphase reactive interface. Long-term galvanostatic cycling tests were performed on the ZABs at various current densities from 5.0 to 50.0 mA cm^{-2}. As shown in **Figure 5**a, the ZAB based on Asy-cathode delivered discharge and charge voltages of 1.12 and 1.93 V at 5.0 mA cm^{-2}, respectively, after the initial activation process. Both the discharge and charge voltages exhibited excellent stability, with the voltage gap increasing slightly from 0.81 to 0.83 V after 2000 cycles (≈333 h). In contrast, the cycling performance of the ZAB based on Con-cathode suffered from heavy decay after approximately 650 cycles, probably due to exfoliation and destruction of the electrocatalysts. This difference in cycling durability is mainly attributed to the distinct electrocatalyst loading structures, with the in situ growth mode of Asy-cathode also providing additional stability. At higher current densities, the Asy-cathode still shows stable cycling behaviors, but the Con-cathode exhibits gradual broadening of the voltage gap (Figure 5a; Figures S14 and S15, Supporting Information). The discharge/charge voltages of the ZABs based on Asy-cathode remained stable for more than 600, 300, and 100 cycles at 10.0, 25.0, and 50.0 mA cm^{-2}, respectively, while those based on Con-cathode only exhibited stability for 200, 80, and 25 cycles, respectively. Therefore, the asymmetric air cathode displays great promise for high-current and long-cycle ZAB applications.

As summarized in Figure 5b, the ratio between the number of stable cycles for the ZABs with Asy-cathode and that for the ZABs with Con-cathode gradually increases with the current density, revealing that the stability of the former cathode is particularly advantageous at high current densities. This behavior indicates that the structure of Con-cathode is quickly destroyed at high currents, while the Asy-cathode resists destruction. Taking the discharge/charge behavior of the ZAB with Asy-cathode at 10.0 mA cm^{-2} as an example, a very stable average voltage gap was delivered during each cycle stage, with a variation of less than 20 mV over 600 cycles (Figure 5c). Furthermore, the 3D multiphase interface of Asy-cathode was well maintained, as evidenced by SEM images (inset of Figure 5c; Figure S16, Supporting Information).

The outstanding mechanical stability of the electrocatalysts in the asymmetric air cathode is obviously attributable to the dynamically stable reactive interface as well as the in situ growth mode. We also performed an XPS analysis of the above cycled Asy-cathode to evaluate its chemical stability. The XPS survey spectrum of the cycled Asy-cathode is similar to that of the pristine Asy-cathode (Figure S17, Supporting Information). The Ni/Fe atomic ratio changed from 2.67 to 2.54 after cycling, indicating a slightly altered but generally stable composition. High-resolution XPS spectra were analyzed to reveal further information about the chemical states. The Ni 2p spectrum of the pristine Asy-cathode exhibits two peaks

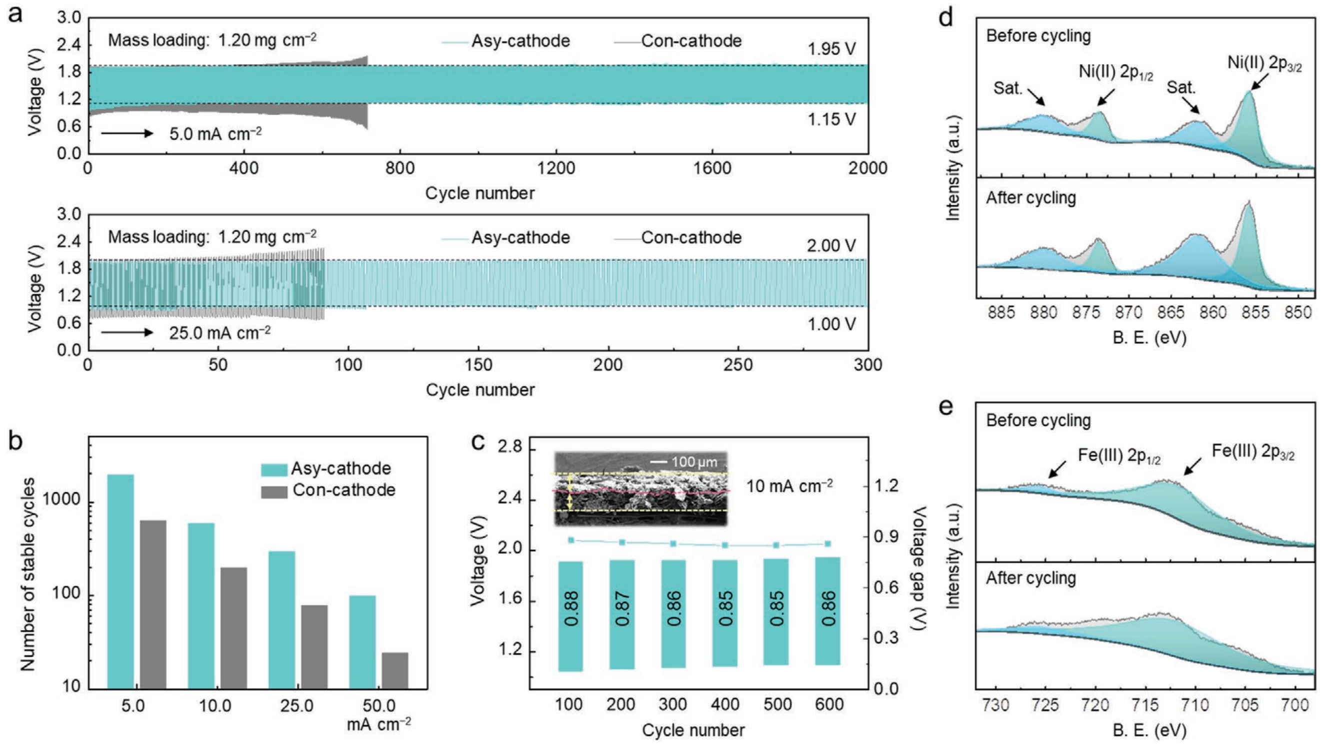

Figure 5. Stability of the ZABs with Asy-cathode and Con-cathode. a) Long-term galvanostatic cycling tests at current densities of 5.0 and 25.0 mA cm^{-2}. b) Numbers of stable cycles at various current densities. c) Average discharge/charge voltages and voltage gaps during each cycling stage of the ZAB with Asy-cathode, at 10.0 mA cm^{-2} (inset: cross-sectional SEM image of Asy-cathode after cycling). d) Ni 2p and e) Fe 2p XPS spectra of Asy-cathode before and after cycling.

with binding energies (BE) of 855.7 and 873.3 eV, which correspond to Ni(II) $2p_{3/2}$ and Ni(II) $2p_{1/2}$ respectively, accompanied by satellite peaks (Figure 5d).[25] Similarly, the Fe 2p spectrum of the pristine Asy-cathode exhibits Fe(III) $2p_{3/2}$ and Fe(III) $2p_{1/2}$ peaks (Figure 5e).[26] The chemical states of Ni and Fe remained essentially stable after cycling, indicating the high chemical resistance of Asy-cathode, which can provide stable electrocatalytic active sites during long-term cycling processes.

ZABs based on our asymmetric air cathode display multiple advantages including a low overpotential, a high energy efficiency, a high power density, and superior long-term stability. These beneficial properties are mainly attributed to the cathode architecture based on the 3D reactive interface strategy. More specifically, the remarkable performance originates from synergistic effects of several factors. 1) The asymmetric architecture provides a 3D multiphase reactive interface that guarantees a sufficient amount of electrocatalytic active sites inside the cathode rather than on its surface, thus enhancing electrocatalytic activity. 2) Mass transfer and electron conduction are accelerated by the easier access of hydroxyl ions and oxygen to the interior of the porous conductive skeleton, which favors a high current capability. 3) The dynamically stable reactive interface and in situ growth mode enhance the ability of the electrocatalysts to endure long-term and high-current cycling, leading to greatly improved durability. 4) The in situ growth mode also promotes electron conduction. Thus, the proposed air cathode design based on asymmetric architecture simultaneously enhances the reaction kinetics and cycling durability of ZABs by improving the multiphase interface. Herein, the performance of NiFe-LDH as a model electrocatalyst in the asymmetric air cathode was obviously improved compared with that in the corresponding conventional air cathode. By altering the electrocatalyst, different asymmetric cathodes with better electrocatalytic performance or a specific functionality could be achieved.

In summary, in allusion to the poor reactive interfaces and insufficient active sites in conventional air cathodes, an asymmetric air cathode design for rechargeable ZABs is proposed. The asymmetric growth of electrocatalysts inside the cathode generated a 3D multiphase reactive interface, which greatly increased the amount of functional active sites, accelerated mass transfer, and strengthened the interfacial stability. Consequently, a reduced overpotential, a higher power density, and a longer lifespan were obtained for the ZABs based on an Asy-cathode. This work provides a versatile strategy for improving the interfacial reaction kinetics of air cathodes, which is instructive to the future electrode design for next-generation metal–air batteries with high-current and long-cycle energy storage applications.

Supporting Information

Supporting Information is available from the Wiley Online Library or from the author.

Acknowledgements

This work was supported by National Key Research and Development Program (2016YFA0202500 and 2016YFA0200102), National Natural Science Foundation of China (21905157, 21676160, 21825501, and U1801257), China Postdoctoral Science Foundation (2019M650697), and the Tsinghua University Initiative Scientific Research Program. The authors thank Ding Ren, Dr. Cheng Tang, Dr. Hao-Fan Wang, Dr. Bin Wang, and Prof. Jia-Qi Huang for helpful discussions.

Conflict of Interest

The authors declare no conflict of interest.

Keywords

3D multiphase interfaces, air cathodes, asymmetric architecture, zinc–air batteries

Received: December 27, 2019
Revised: January 23, 2020

---

[1] a) Y. R. Liang, C.-Z. Zhao, H. Yuan, Y. Chen, W. C. Zhang, J.-Q. Huang, D. S. Yu, Y. L. Liu, M.-M. Titirici, Y.-L. Chueh, H. J. Yu, Q. Zhang, *InfoMat* **2019**, *1*, 6; b) B.-Q. Li, S.-Y. Zhang, B. Wang, Z.-J. Xia, C. Tang, Q. Zhang, *Energy Environ. Sci.* **2018**, *11*, 1723.

[2] a) Y. G. Li, H. J. Dai, *Chem. Soc. Rev.* **2014**, *43*, 5257; b) J. Pan, Y. Y. Xu, H. Yang, Z. H. Dong, H. F. Liu, B. Y. Xia, *Adv. Sci.* **2018**, *5*, 1700691.

[3] M. J. Wu, G. X. Zhang, M. H. Wu, J. Prakash, S. H. Sun, *Energy Storage Mater.* **2019**, *21*, 253.

[4] a) X. Y. Cai, L. F. Lai, J. Y. Lin, Z. X. Shen, *Mater. Horiz.* **2017**, *4*, 945; b) J. T. Zhang, Z. H. Zhao, Z. H. Xia, L. M. Dai, *Nat. Nanotechnol.* **2015**, *10*, 444.

[5] a) Y. P. Zhu, Y. Jing, A. Vasileff, T. Heine, S. Z. Qiao, *Adv. Energy Mater.* **2017**, *7*, 1602928; b) T. Y. Ma, J. L. Cao, M. Jaroniec, S. Z. Qiao, *Angew. Chem., Int. Ed.* **2016**, *55*, 1138; c) W. Xia, R. Q. Zou, L. An, D. G. Xia, S. J. Guo, *Energy Environ. Sci.* **2015**, *8*, 568; d) Y. Pan, S. J. Liu, K. A. Sun, X. Chen, B. Wang, K. L. Wu, X. Cao, W. C. Cheong, R. G. Shen, A. J. Han, Z. Chen, L. R. Zheng, J. Luo, Y. Lin, Y. Q. Liu, D. S. Wang, Q. Peng, Q. Zhang, C. Chen, Y. D. Li, *Angew. Chem., Int. Ed.* **2018**, *57*, 8614; e) B. Lv, S. Zeng, W. Yang, J. Qiao, C. Zhang, C. F. Zhu, M. H. Chen, J. T. Di, Q. W. Li, *J. Energy Chem.* **2019**, *38*, 170.

[6] a) C. Tang, B. Wang, H.-F. Wang, Q. Zhang, *Adv. Mater.* **2017**, *29*, 1703185; b) H.-F. Wang, C. Tang, B. Wang, B.-Q. Li, Q. Zhang, *Adv. Mater.* **2017**, *29*, 1702327; c) J. Yin, B. B. Wei, Y. X. Li, Y. F. Li, P. X. Xi, *J. Energy Chem.* **2019**, *34*, 1; d) L. T. Ma, S. M. Chen, Z. X. Pei, H. F. Li, Z. F. Wang, Z. X. Liu, Z. J. Tang, J. A. Zapien, C. Y. Zhi, *ACS Nano* **2018**, *12*, 8597.

[7] a) C. Tang, H.-F. Wang, Q. Zhang, *Acc. Chem. Res.* **2018**, *51*, 881; b) H.-F. Wang, C. Tang, Q. Zhang, *Adv. Funct. Mater.* **2018**, *28*, 1803329.

[8] a) Y. Q. Wang, Y. Q. Zou, L. Tao, Y. Y. Wang, G. Huang, S. Q. Du, S. Wang, *Nano Res.* **2019**, *12*, 2055; b) Y. J. Li, H. C. Zhang, T. H. Xu, Z. Y. Lu, X. C. Wu, P. B. Wan, X. M. Sun, L. Jiang, *Adv. Funct. Mater.* **2015**, *25*, 1737; c) M. C. Luo, Z. L. Zhao, Y. L. Zhang, Y. J. Sun, Y. Xing, F. Lv, Y. Yang, X. Zhang, S. Hwang, Y. N. Qin, J. Y. Ma, F. Lin, D. Su, G. Lu, S. J. Guo, *Nature* **2019**, *574*, 81; d) D. X. Ji, L. Fan, L. L. Li, S. J. Peng, D. S. Yu, J. N. Song, S. Ramakrishna, S. J. Guo, *Adv. Mater.* **2019**, *31*, 1808267.

[9] Y. B. Li, J. Fu, C. Zhong, T. P. Wu, Z. W. Chen, W. B. Hu, K. Amine, J. Lu, *Adv. Energy Mater.* **2019**, *9*, 1802605.

[10] a) X. Q. Wu, F. Y. Chen, Y. C. Jin, N. Zhang, R. L. Johnston, *ACS Appl. Mater. Interfaces* **2015**, *7*, 17782; b) S. Chen, J. J. Duan, P. J. Bian, Y. H. Tang, R. K. Zheng, S. Z. Qiao, *Adv. Energy Mater.* **2015**, *5*, 1500936.

[11] J. Pampel, T. P. Fellinger, *Adv. Energy Mater.* **2016**, *6*, 1502389.

[12] F. L. Meng, H. X. Zhong, D. Bao, J. M. Yan, X. B. Zhang, *J. Am. Chem. Soc.* **2016**, *138*, 10226.

[13] a) J. L. Liu, D. D. Zhu, Y. Zheng, A. Vasileff, S. Z. Qiao, *ACS Catal.* **2018**, *8*, 6707; b) J. L. Liu, Y. Zheng, Z. Y. Wang, Z. G. Lu, A. Vasileff, S. Z. Qiao, *Chem. Commun.* **2018**, *54*, 463.

[14] a) M. Gong, H. J. Dai, *Nano Res.* **2015**, *8*, 23; b) Y. Jia, L. Z. Zhang, G. P. Gao, H. Chen, B. Wang, J. Z. Zhou, M. T. Soo, M. Hong, X. C. Yan, G. R. Qian, J. Zou, A. J. Du, X. D. Yao, *Adv. Mater.* **2017**, *29*, 1700017.

[15] C. Andronescu, S. Seisel, P. Wilde, S. Barwe, J. Masa, Y. T. Chen, E. Ventosa, W. Schuhmann, *Chem. – Eur. J.* **2018**, *24*, 13773.

[16] Z. Qiu, C. W. Tai, G. A. Niklasson, T. Edvinsson, *Energy Environ. Sci.* **2019**, *12*, 572.

[17] M. Qiao, C. Tang, L. C. Tanase, C. M. Teodorescu, C. M. Chen, Q. Zhang, M.-M. Titirici, *Mater. Horiz.* **2017**, *4*, 895.

[18] P. S. Li, X. X. Duan, Y. Kuang, Y. P. Li, G. X. Zhang, W. Liu, X. M. Sun, *Adv. Energy Mater.* **2018**, *8*, 1703341.

[19] Y. H. Qian, T. An, E. Sarnello, Z. L. Liu, T. Li, D. Zhao, *ACS Appl. Energy Mater.* **2019**, *2*, 1784.

[20] S. D. Wang, H. L. Jiang, L. Song, *Batteries Supercaps* **2019**, *2*, 509.

[21] J. Fu, Z. P. Cano, M. G. Park, A. P. Yu, M. Fowler, Z. W. Chen, *Adv. Mater.* **2017**, *29*, 1805230.

[22] H. Fan, Y. Wang, F. J. Gao, L. Q. Yang, M. Liu, X. Du, P. Wang, L. J. Yang, Q. Wu, X. Z. Wang, Z. Hu, *J. Energy Chem.* **2019**, *34*, 64.

[23] Z. Zhang, Y. P. Deng, Z. Y. Xing, D. Luo, S. Sy, Z. P. Cano, G. H. Liu, Y. Jiang, Z. W. Chen, *ACS Nano* **2019**, *13*, 7062.

[24] J. B. Zhu, M. L. Xiao, Y. L. Zhang, Z. Jin, Z. Q. Peng, C. P. Liu, S. L. Chen, J. J. Ge, W. Xing, *ACS Catal.* **2016**, *6*, 6335.

[25] M. F. Qiao, Y. Wang, T. Wågberg, M. Mamat, X. Hu, G. A. Zou, G. Z. Hu, *J. Energy Chem.* **2020**, *47*, 146.

[26] Y. J. Li, L. Cui, P. F. Da, K. W. Qiu, W. J. Qin, W. B. Hu, X. W. Du, K. Davey, T. Ling, S. Z. Qiao, *Adv. Mater.* **2018**, *30*, 1804653.